Journal of Vacuum Science and Technology A

RESEARCH ARTICLE | FEBRUARY 27 2024

High crystalline quality homoepitaxial Si-doped β-Ga_2O_3(010) layers with reduced structural anisotropy grown by hot-wall MOCVD

Special Collection: Gallium Oxide Materials and Devices

D. Gogova ; D. Q. Tran ; V. Stanishev ; V. Jokubavicius; L. Vines ; M. Schubert ; R. Yakimova; P. P. Paskov ; V. Darakchieva

J. Vac. Sci. Technol. A 42, 022708 (2024)
https://doi.org/10.1116/6.0003424

JVST A
Journal of Vacuum Science & Technology A

ARTICLE

pubs.aip.org/avs/jva

High crystalline quality homoepitaxial Si-doped β-Ga_2O_3(010) layers with reduced structural anisotropy grown by hot-wall MOCVD

Cite as: J. Vac. Sci. Technol. A **42**, 022708 (2024); doi: 10.1116/6.0003424
Submitted: 25 December 2023 · Accepted: 29 January 2024 ·
Published Online: 27 February 2024

D. Gogova,[1,a)] D. Q. Tran,[1,2] V. Stanishev,[1] V. Jokubavicius,[1,2] L. Vines,[3] M. Schubert,[4,5] R. Yakimova,[1] P. P. Paskov,[1,2] and V. Darakchieva[1,2,4,a)]

AFFILIATIONS

[1]Department of Physics, Chemistry and Biology, Linköping University, 581 83 Linköping, Sweden
[2]Center for III-Nitride Technology—C3NiT-Janzèn, Linkping University, 581 83 Linköping, Sweden
[3]Department of Physics, Oslo University, 0316 Oslo, Norway
[4]NanoLund, Center for III-Nitride Technology—C3NiT-Janzèn and Terahertz Materials Analysis Center (TheMAC), Lund University, P. O. Box 118, 221 00 Lund, Sweden
[5]Department of Electrical and Computer Engineering, University of Nebraska-Lincoln, Lincoln, Nebraska 68588

Note: This paper is part of the Special Topic Collection on Gallium Oxide Materials and Devices.
a)Authors to whom correspondence should be addressed: daniela.gogova@liu.se and vanya.darakchieva@ftf.lth.se

ABSTRACT

A new growth approach, based on the hot-wall metalorganic chemical vapor deposition concept, is developed for high-quality homoepitaxial growth of Si-doped single-crystalline β-Ga_2O_3 layers on (010)-oriented native substrates. Substrate annealing in argon atmosphere for 1 min at temperatures below 600 °C is proposed for the formation of epi-ready surfaces as a cost-effective alternative to the traditionally employed annealing process in oxygen-containing atmosphere with a time duration of 1 h at about 1000 °C. It is shown that the on-axis rocking curve widths exhibit anisotropic dependence on the azimuth angle with minima for in-plane direction parallel to the [001] and maximum for the [100] for both substrate and layer. The homoepitaxial layers are demonstrated to have excellent structural properties with a β-Ga_2O_3(020) rocking curve full-widths at half-maximum as low as 11 arc sec, which is lower than the corresponding one for the substrates (19 arc sec), even for highly Si-doped (low 10^{19} cm^{-3} range) layers. Furthermore, the structural anisotropy in the layer is substantially reduced with respect to the substrate. Very smooth surface morphology of the epilayers with a root mean square roughness value of 0.6 nm over a $5 \times 5\,\mu m^2$ area is achieved along with a high electron mobility of 69 $cm^2\,V^{-1}\,s^{-1}$ at a free carrier concentration $n = 1.9 \times 10^{19}$ cm^{-3}. These values compare well with state-of-the-art parameters reported in the literature for β-Ga_2O_3(010) homoepitaxial layers with respective Si doping levels. Thermal conductivity of 17.4 $Wm^{-1}K^{-1}$ is determined along the [010] direction for the homoepitaxial layers at 300 K, which approaches the respective value of bulk crystal (20.6 $Wm^{-1}K^{-1}$). This result is explained by a weak boundary effect and a low dislocation density in the homoepitaxial layers.

I. INTRODUCTION

Although known since decades, only recently III-sesquioxides (gallium and indium oxides) have been re-discovered as a new class of highly prospective wide bandgap semiconductors. In the past, polycrystalline highly doped In_2O_3 or β-Ga_2O_3 were used as high-conductivity materials for transparent electrodes in "smart windows," photovoltaics, as well as in gas sensors.[1–7] During the last decade, significant research efforts have been focused on growth of single-crystalline III-sesquioxides layers with low defect densities and on demonstration of high-performance devices on their basis. The thermodynamically stable β-Ga_2O_3 polytype has a ultra-wide bandgap of 4.7–5.04 eV,[8,9] which makes it promising for applications in short

wavelength photonics and transparent electronics.[10–13] β-Ga_2O_3 also has a high breakdown electric field of 8 MV cm^{-1}, which exceeds those of technologically relevant semiconductors such as Si, GaAs, SiC, and GaN, rivaled only by diamond. Consequently, there is a tremendous potential of β-Ga_2O_3 for high-power electronics applications.[14,15] Indeed, Baliga's figure of merit for β-Ga_2O_3 is several times larger than those for 4H-SiC and GaN.[14,15] Furthermore, β-Ga_2O_3 possesses better radiation stability in comparison to GaN[16–18] and hence can find application in very harsh environments.[19] Consequently, the unique properties of this material, combined with the availability of simple and low cost, in comparison to vapor phase grown GaN and AlN substrates, melt growth methods for large-scale production of bulk crystals[14,20,21] have made β-Ga_2O_3 a strong candidate for next generation high-power electronics for green and sustainable development.

The metalorganic chemical vapor deposition (MOCVD) technique, which is the growth method of choice in this work, exhibits excellent reproducibility and can be scaled up for high volume production. Homoepitaxial high-quality growth with fast rates represents one of the most significant challenges for further adoption of β-Ga_2O_3 in electronics. Homoepitaxial β-Ga_2O_3 layers with controlled doping and with different surface crystallographic orientations, e.g., (100), (010), (001), and (−201) have been demonstrated by MOCVD.[22–30] The (010)-oriented β-Ga_2O_3 epitaxial layers have been shown to exhibit higher electron mobilities as compared to other orientations[31] and hence they are preferred for device fabrication. The MOCVD has demonstrated promising electronic transport properties of β-Ga_2O_3 (010) layers with a room temperature mobility of 184 $cm^2\ V^{-1}\ s^{-1}$ at a free electron concentration of 2.75×10^{16} cm^{-3},[26] approaching the predicted theoretical limit of approximately 200 $cm^2\ V^{-1}\ s^{-1}$.[32] The concentration of the compensation defects in these layers was estimated to be as low as 9.4×10^{14} cm^{-3}, which is significantly lower than what was observed for β-Ga_2O_3 grown by other epitaxial methods.[29,33] Despite these promising results, β-Ga_2O_3 homoepitaxial layers grown on (010) substrates typically show a rougher surface morphology mainly caused by the formation of (110) and (−110) facets along the [001] direction during growth.[25,34] The growth temperature strongly influences the surface morphology of β-Ga_2O_3 as it plays a crucial role in adatom diffusion at the growth surface. It has been reported that high growth temperatures (~880 °C) were required in order to ensure a uniform and smooth surface while temperatures lower than 800 °C resulted in a rougher surface with visible macroscopic dents.[26] On the other hand, atomically flat surfaces of β-Ga_2O_3 (010) homoepitaxial layers at growth temperatures below 700 °C with fairly good transport properties have been demonstrated.[35] We note that lower growth temperatures are desirable to reduce the energy consumption during the MOCVD process. In this respect, it is worth mentioning that we have recently reported hetero- and homoepitaxial β-Ga_2O_3 (−201) epitaxial layers with state-of-the-art properties grown by hot-wall MOCVD at reduced temperatures (740 °C).[27] The hot-wall MOCVD concept has been proven to be very effective in growth of SiC and III-N materials and multilayer heterostructures of high quality[36–38] and superior device performance[39–42] have been demonstrated. Compared to the conventional cold-wall MOCVD with heated substrates holder only,[22–24,26] the hot-wall MOCVD employs a heated susceptor providing highly uniform temperature distribution in the growth zone vertically and laterally, which facilitates high cracking efficiency of the precursors preventing growth-limited species consumption by gas-phase adduct formation.

The goal of this study is to explore hot-wall MOCVD for the homoepitaxial growth of Si-doped β-Ga_2O_3 (010) and to gain insights into material structural quality and as well as in transport properties and thermal conductivity.

II. EXPERIMENT

Commercial edge-defined film-fed grown (EFG) Fe-doped semi-insulating β-Ga_2O_3 (010)-oriented substrates were employed for homoepitaxial growth. The substrates were cleaned by a standard chemical procedure before annealing and deposition. Trimethylgallium (TMGa) was used as a gallium precursor due to the high vapor pressure, providing large growth rates needed for a large-scale device fabrication. For *n*-type doping, a diluted silane (SiH_4, 10 ppm in Ar) as a source of the shallow donor silicon was used.

For the study of epi-ready surface formation, the substrates were annealed in an induction heated quartz tube furnace operating at 28 kHz. The quartz tube provides a closed volume which can be evacuated down to 10^{-5} mbar by turbo pump and has inlet and outlet for process gases. β-Ga_2O_3 substrates were kept in a graphite container made of high-purity, high-density graphite wrapped with rigid graphite insulation. The temperature was measured on the outer surface of the graphite container using an infrared pyrometer. The temperature inside the container was estimated using the STR VIRTUAL REACTOR software based on the measured temperature on the outer surface of the graphite container. Before each annealing experiment, the quartz tube was evacuated to 10^{-5} mbar and filled with a high purity Ar (6N) to establish a pressure of 900 mbar. This pressure was maintained during the entire annealing experiment. In the course of annealing, the temperature was increased with a heating rate of 25 °C/min from room to the desired annealing temperature, which was varied from 500 to 700 °C. The annealing time was set to 1 min for all experiments. After the annealing, the induction heating was switched off and the furnace and samples were left to cooldown. The average cooling rate was about 30 °C/min.

A horizontal hot-wall MOCVD reactor (Epiluvac AB) was employed for β-Ga_2O_3 homoepitaxial growth.[27] The growth parameters have been optimized similar to those in our previous study[27] for deposition of high crystalline quality (−201)-oriented β-Ga_2O_3 heteroepitaxial and homoepitaxial layers. The following set of growth parameters were selected: deposition temperature of 740 °C, growth pressure of 50 mbar, TMGa flow of 0.75 ml/min, and O_2 to TMGa ratio of 265. The bubbler was kept at (5 ± 0.1) °C. Argon gas of high purity (5N) was used as a carrier gas and for reagent dilution. Before the growth, epi-ready surfaces of the β-Ga_2O_3 (010) substrates were prepared by annealing in Ar atmosphere at 575 °C for 1 min in a dedicated furnace as described above. Homoepitaxial Si-doped layers with thicknesses of 540 nm were grown within 1 h targeting [Si] of $\geq 1 \times 10^{19}$ cm^{-3}.

Different analytical methods were employed to characterize the morphological, structural, compositional, electrical, and

thermal properties of the material grown. The Si concentration was determined by secondary ion mass spectrometry (SIMS) using a Cameca IMS7f with a 10 keV O2+ primary beam raster scanned over an area of 150 × 150 μm^2 was used to obtain concentration vs depth profiles for Si. The craters were measured with a Dektak 8 stylus profilometer to calibrate the depth, and a constant sputter rate was assumed. A β-Ga_2O_3 reference sample implanted with ^{28}Si was used to calibrate the concentration. The crystal orientation and the quality of the grown layers were determined by x-ray diffraction (XRD). 2θ-ω scans were performed in an x-ray powder diffraction X' celerator (Panalytical) with a Bragg–Brentano configuration. Rocking curves (RCs) and reciprocal space maps (RSMs) were measured with a high-resolution XRD (HR-XRD) diffractometer Empyrean (Panalytical) using a 2-bounce Ge (220) monochromator as incident-beam optics and a 3-bounce Ge (220) detector. Surface morphology was studied by atomic force microscopy (AFM). The free electron concentration and mobility parameters were determined by electrical Hall effect and generalized infrared spectroscopic ellipsometry (gIRSE) measurements at room temperature. In addition, the thickness of the β-Ga_2O_3 homoepitaxial layers was obtained from the gIRSE data analysis. The Hall-effect measurements were performed in Van der Pauw configuration with a Linseis CS1 instrument. For this purpose, Ti/Au (10 nm/200 nm) ohmic contacts were deposited by thermal evaporation. gIRSE measurements were performed using a rotating compensator Fourier transform infrared ellipsometer (J. A. Woollam Co., Inc.) in the spectral range of 333–1300 cm^{-1} with a spectral resolution of 2 cm^{-1} and at angles of incidence of $\Phi_a = 50°$ and 70°. All measurements are reported as Mueller matrix elements M_{ij}. All elements are normalized by M_{11}. Data are measured at three different sample azimuth positions (in-plane rotations within the sample surface relative to the plane of incidence), separated by 45° offset each. Thermal conductivity measurements were performed by transient thermoreflectance (TTR). In this technique, the sample is heated by a pump laser through gold (Au) transducer layers with a thickness of 100 ± 5 nm deposited on the sample surface. The decay of the sample temperature after pump laser pulses is monitored by measuring the reflectance of the probe laser. The spot size of the probing laser is small enough compared with that of the pump laser to ensure that the heat transport along the surface normal is only probed. The thermal conductivity was obtained via a least-squares fit of the reflectance transients of the probe laser with the solution of the one-dimensional heat transport equation. In this fit, the thermal conductivity of Au[43] and the specific heat of Au[44] and β-Ga_2O_3[45] were used as input parameters. The thermal conductivity of a bare β-Ga_2O_3 (010) substrate was initially measured. Details of the TTR measurement and data analysis can be found elsewhere.[46,47]

III. RESULTS AND DISCUSSION

A. Substrate preparation and surface morphology

We have applied a new approach to prepare the substrate surface by annealing in Ar atmosphere as described above. The surface morphology after the annealing process is summarized in Fig. 1. It illustrates the changes of surface morphology development of the as-received β-Ga_2O_3 (010) substrate [Fig. 1(a)] after annealing at different temperatures [Figs. 1(b)–1(e)]. The surface of the as-received substrate is very smooth but contains small round islands, which are randomly distributed. The surface roughness is increasing with increasing temperature as a result of surface restructuring and reformation. Steps start to appear on the surface at a temperature of 575°C and which are maintained at higher annealing temperatures up to 700 °C. However, the surface becomes significantly rougher for annealing temperatures of 600 and 700°C [Figs. 1(d) and 1(e)], which might be attributed to partial decomposition of the surface and/or enhanced step bunching. The temperature treatment at 575 °C is the best suited for the formation of epi-ready stepped surface with regular steps and fairly small root mean square (RMS) roughness of 0.2 nm [Fig. 1(c)]. The method for surface preparation proposed here is highly efficient and cost-effective because lower temperatures (below 600 °C) and a short treatment time (1 min) are employed in comparison to the typically implemented annealing procedures of oxide substrates, including β-Ga_2O_3, ZnO, and sapphire, performed at about 1000 °C for 1 h in oxygen-containing atmosphere.[22,24,48–51] The use of Ar gas at rather high pressure is beneficial for the surface processes avoiding surface erosion reactions and slowing down surface diffusion, thus resulting in surface steps formation with sufficient height to ensure small surface roughness.[52] Since the growth takes place at a higher temperature than the optimal annealing temperature for surface pre-treatment of 575 °C, we also provide an AFM image of the substrate annealed for 1 h at the growth conditions at a temperature of 740 °C and 50 mbar Ar pressure [Fig. 1(f)] for comparative reasons. It can be seen that although the surface roughness is similar, i.e., 0.2 nm to the case of optimal annealing [Fig. 1(c)], no steps have formed at the surface of the *in situ* annealed substrate [Fig. 1(f)]. The reason is that in this case the Ar pressure is significantly lower, 50 mbar as compared to the nearly 1 atmosphere for the pre-treatment process.

The as-prepared substrates, thermally treated at 575°, were loaded in the hot-wall MOCVD reactor and homoepitaxial growth was performed. The whole set of deposition parameters was optimized in terms of attainment of high crystalline quality of the material grown and formation of a smooth surface morphology as required for growth of complete device structures and processing. Representative AFM images of a single-crystalline Si-doped β-Ga_2O_3 (010) layer grown with the optimized conditions are shown in Fig. 1(g) and 1(h). A very smooth surface with an RMS roughness of 0.6 nm over a 5 × 5 μm^2 and 0.8 nm over a 10 × 10 μm^2 areas are obtained, which are among the best RMS values reported in the literature so far.[22,23,25–27] We note that a homoepitaxial layer grown simultaneously on a substrate that is annealed at 740° at 50 mbar, i.e., at the growth conditions for 1 h, has an increased surface roughness by 35%–50% [Figs. 1(i) and 1(j)] in comparison to the layer grown on the optimized low-temperature *ex situ* annealing [Figs. 1(g) and 1(h)].

B. Structural properties

2θ-ω scans of the homoepitaxial layers were measured in a wide range of 2θ angle from 10° to 90°. A representative spectrum shown in Fig. 2 reveals a single Bragg peak indexed to the (020) plane of the β-Ga_2O_3 crystal, indicating homoepitaxial growth of

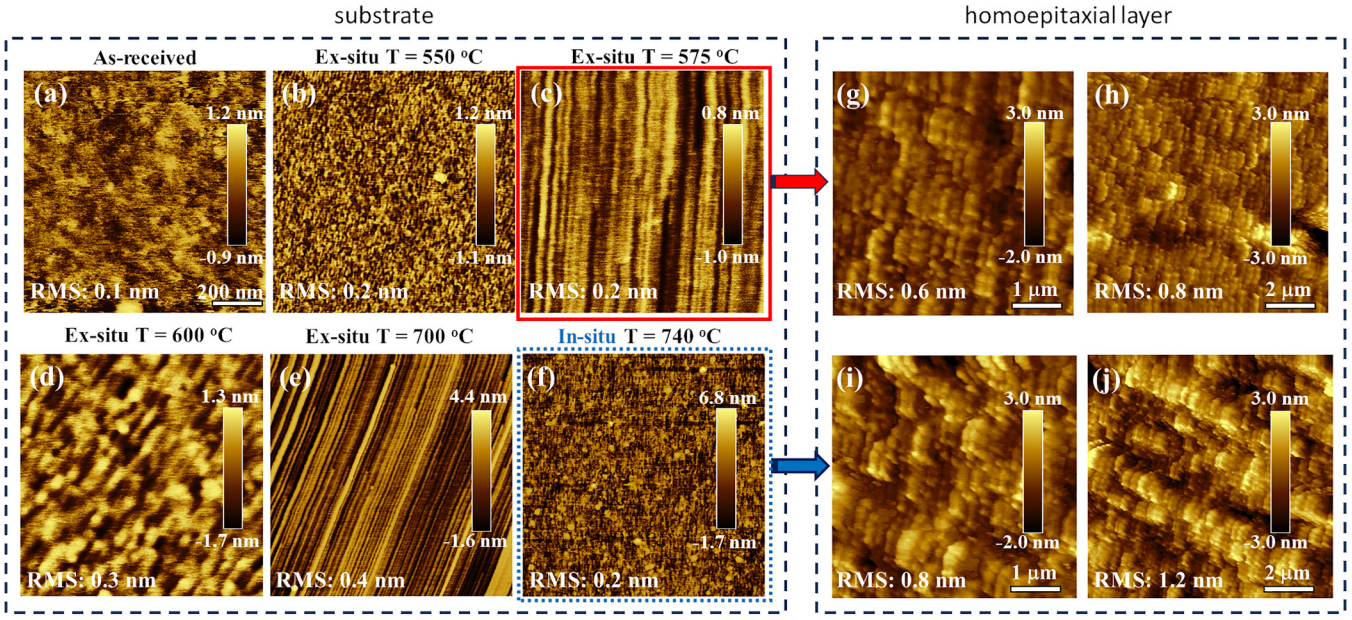

FIG. 1. Representative $1\times 1\,\mu m^2$ AFM images of (010)-oriented β-Ga_2O_3 substrates. (a)–(f) As-received (a) and annealed *ex situ* in Ar atm (900 mbar) at 550 (b), 575 (c), 600 (d), and 700 °C (e) for 1 min and *in situ* at the growth conditions of 50 mbar Ar, 740 °C for 1 h (f). The scale indicated in (a) is the same for (b)–(f). The red frame in (c) marks the image of the substrate annealed at optimal conditions, and the blue dotted frame indicates the respective image of the *in situ* annealed substrate at growth conditions (f). Representative $5\times 5\,\mu m^2$ [(g) and (i)] and $10\times 10\,\mu m^2$ [(h) and (j)] AFM image of homoepitaxial Si-doped β-Ga_2O_3 (010) layers grown simultaneously at optimized conditions on *ex situ* optimal pre-treated substrates [(g) and (h)] and annealed at growth conditions substrate [(i) and (j)].

the layer with a substrate-driven orientation and a similar out-of-plane lattice parameter as the substrate.

HR-XRD RCs of the symmetric (020) diffraction peak were measured at different azimuth angles (φ) over a range of 360° with a step of 20° for both homoepitaxial layers and substrate. The $\varphi = 0°$ is always set such as the x-ray beam projection is parallel to β-Ga_2O_3 [001] [Fig. 3(b)]. The full-width at half maximum (FWHM) of the RCs for a representative β-Ga_2O_3 (010)

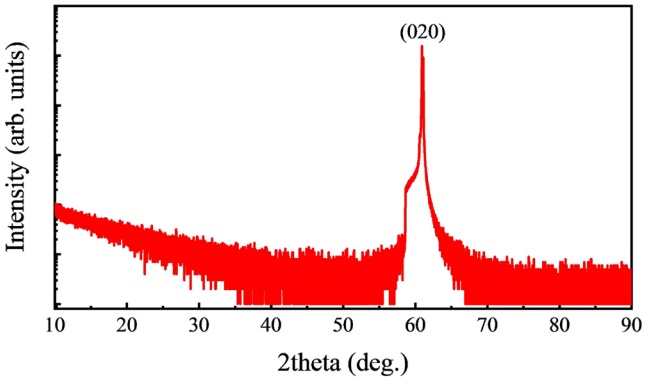

FIG. 2. Representative 2θ-ω scan of the Si-doped homoepitaxially grown layer.

homoepitaxial layer and the substrate is shown in Fig. 3(b) as a function of the azimuth position. Both the layer and the substrate show RC broadening that is strongly dependent on the azimuth orientation with a minimum value for azimuth direction parallel to the [001] crystallographic direction and the maximum FWHM when the beam projection is parallel to the [100]. In general, broadening of the symmetric RCs can be due to tilt of the single crystalline domains associated with dislocations, limited lateral coherence length as a result of defects such as stacking faults, wafer curvature, or surface roughness.[53] Previously, in-plane structural anisotropy of the on-axis RC FWHM has been observed for bulk β-Ga_2O_3 (-201) and attributed to anisotropy in the lateral coherence lengths associated with stacking faults and grain boundaries.[54]

Exemplary RCs measured at $\varphi = 0°$, 40°, 80°, and 120° for the substrate and a homoepitaxial layer are shown in Figs. 3(c) and 3(d), respectively. As the azimuth position changes, the (020) RC first noticeably broadens and then develops a clear multiple peak structure, which is most pronounced at $\varphi = 120°$, for both substrate and layer. The multi-peak structure of the RCs indicates that most likely the reason for the anisotropic broadening is a tilt toward β-Ga_2O_3 [100]. In general, a larger curvature in that direction could also cause the observed RC shape as a result of the different thermal expansion coefficient along the two in-plane directions. Since the thermal expansion coefficient along the [100] is ≈20% lower than the one along [001] less lattice compression along this direction during cooling down as compared to [001] can be expected. However, this effect should be more significant for the

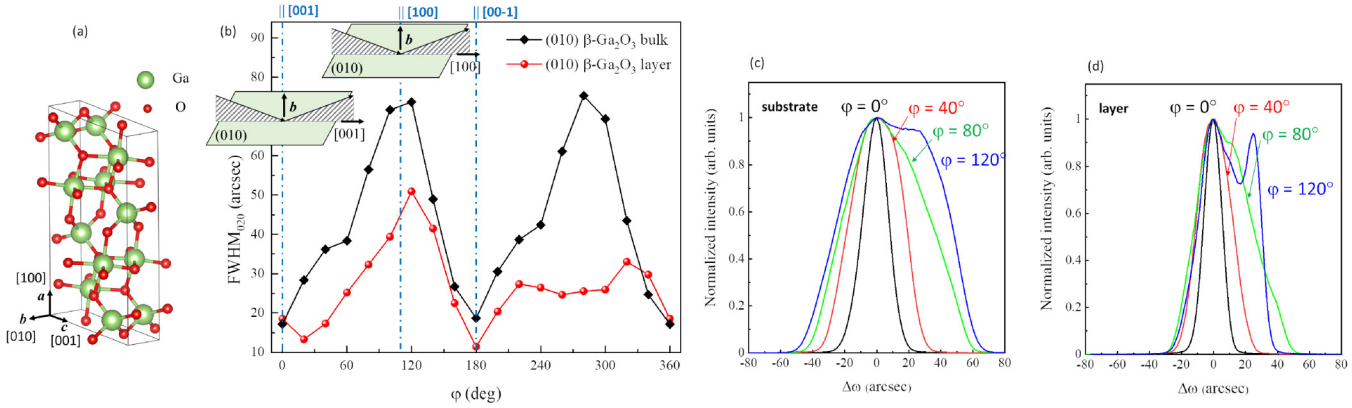

FIG. 3. β-Ga_2O_3 monoclinic crystal structure with main crystallographic directions indicated (a). β-Ga_2O_3 (010) RC FWHM as a function of azimuth orientation φ for a representative homoepitaxial layer and the substrate (b). At $\varphi = 0°$, the azimuthal direction is parallel to the β-Ga_2O_3 [001] and at $\varphi = 111.7°$ to the β-Ga_2O_3 [100] as indicated in the insets in (b). RCs of the substrate (c) and the homoepitaxial layer (d) measured at different φ angles (0°, 40°, 80°, and 120°).

homoepitaxial layer than for the substrate, which is grown by the edge defined method. In the latter, not sufficient necking and shouldering during initial crystal growth typically leads to twin or poly-grain formation,[55] which could in principle give rise to multi-peak shape of the on-axis RC. We note that the growth direction of the bulk crystal in the edge defined method is along the ⟨010⟩ crystallographic direction. Very high growth rate can lead to a concave growth interface with higher temperature gradients, which may also contribute to anisotropic substrate curvature. Other effects such as anisotropic lateral coherence lengths or extended defects are less likely to be the sole reason for the observed anisotropic RC broadening as they are expected to only lead to broadening not multiple peaks. However, a dedicated investigation is needed to have a more conclusive interpretation.

For the purposes of the current study, it is worth pointing out that the homoepitaxial layer shows a smaller RC broadening compared to that of the substrate for all azimuth angles except at $\varphi = 0°$ [Fig. 3(b)]. For the latter, the 002 RCs have minimum FWHMs with 17 arc sec for the substrate and 18 arc sec for the layer. At the second minimum of $\varphi = 180°$, the layer has a substantially narrower RC of 11 arc sec as compared to the substrate with an FWHM of 19 arc sec [see also Fig. 4(a)]. Even larger differences between layer and substrate are revealed at the maximum FWHMs ($\varphi = 280°$) with 75 arc sec for the substrate and 26 arc sec for the layer [Fig. 3(b)]. In fact, the RC FWHMs of the homoepitaxial layer are expected to be even smaller since the measured RCs of the layer are convolution between the signals from the layer and the substrate. This is supported by grazing incidence measurement of the (421) RCs presented in Fig. 4(b). As the angle of incidence is only 4.6° in this case, the x-ray beam probes primarily the layer due to the low penetration depth and the contribution from the substrate is minimized. The β-Ga_2O_3 (421) RC of the layer is found to be only 34 arc sec as compared to 102 arc sec for the substrate. A possible origin of the large (421) RC broadening for the substrate may be the line-shaped defects, called nanogrooves or nanopipes extending along the [010] crystallographic direction.[55] Typical dimensions of the nanopipes are of dozen nanometers in the [100] direction and hundreds of nanometers in the [001] direction.[56] Our results clearly indicate that the structural quality of the layer is substantially improved and the structural anisotropy is reduced with respect to the substrate.

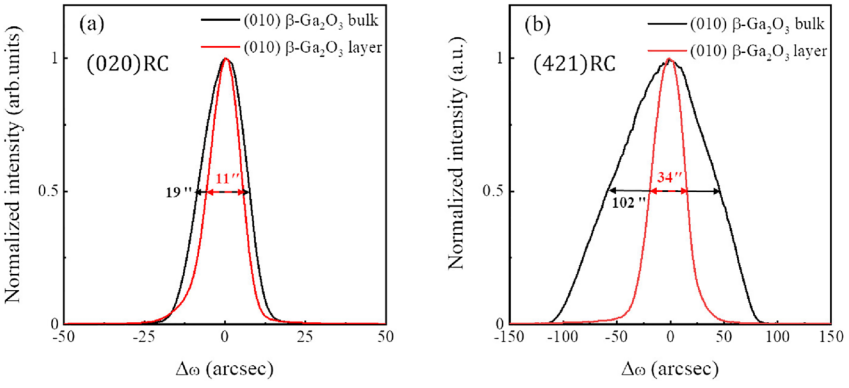

FIG. 4. β-Ga_2O_3 (010) symmetric RCs at $\varphi = 180°$ for a representative homoepitaxial layer and the substrate (a). β-Ga_2O_3 (421) asymmetric RCs of the same representative layer and substrate (b).

C. Free charge carrier properties

In order to determine the free charge carrier properties of the sample, we analyzed the gIRSE data employing the Drude free electron model and accounting for the IR phonon contributions. We used a three-phase optical model consisting of the sequence ambient-layer-substrate. Both layer and substrate were modeled using a dielectric tensor, which renders the infrared optical properties of monoclinic symmetry β-Ga_2O_3. The dielectric function tensor model uses the eigen dielectric displacement vector summation approach as described in Refs. 57 and 58. In this model approach, the contributions of infrared active phonon modes are described by amplitude, frequency, unit vector, and broadening parameters for each of the eight B_u and four A_u symmetry modes polarized either within or perpendicular to the monoclinic lattice plane, respectively. The lattice vectors **a** and **c** define the monoclinic plane. Two different presentations of the model dielectric function tensor exist, one for the transverse optical (TO) and one for the longitudinal optical (LO) lattice excitations. Both forms are invariant and closely related to each other by simple tensor inversion.

Coupling between LO modes and free charge carrier excitations (plasmons) leads to strongly anisotropic and free charge carrier dependent modifications of amplitude, direction, frequency, and broadening of the LO phonon-plasmon coupled modes in β-Ga_2O_3. As a result, the dielectric function tensor changes significantly and permits sensitive determination of the free charge carrier parameters including their direction dependent mobility parameters (μ). These can be rendered along Cartesian axes, for example, along axes **a** (μ_a), **b** (μ_b), and $\mathbf{c}^\star$ ($\mu_{c^\star}$), where $\mathbf{c}^\star$ is reciprocal lattice vector to **c**. It is noted that the Γ-point bottom of the conduction band effective mass parameter is needed in this approach, which was determined independently using the optical Hall effect, as described by Knight *et al.* in Ref. 59. It was further found by Knight *et al.* that the effective electron mass parameter is nearly isotropic. A detailed derivation of the gRISE model function approach and discussion of free charge carrier parameter results are given in Ref. 60. In the present work, the same model approach was used for rendering the frequency dependencies of the infrared dielectric tensor elements for the substrate and the homoepitaxial layer. Both tensors are identical in their phonon mode and orientation parameters but differ in their free charge carrier parameters.

First, the substrate was measured by gIRSE and the free charge carrier parameters were determined. Then, the samples with the epitaxial material were measured. All phonon mode parameters were assumed the same between the substrate and the epitaxial material, and the free charge carrier parameters of the substrate were kept fixed. The relatively low mobility parameters in the substrate may be due to the presence of extended defects and impurities.[55] Then, the only remaining free parameters are the thickness and the free charge carrier parameters of the epitaxial layer. Thereby, density (N) and mobility parameters (μ_a, μ_b, and $\mu_{c^\star}$) are obtained for both substrate and epitaxial layer, in addition to the homoepitaxial layer thickness of 540 nm. The results are summarized in Table I. The best match model calculated and measured gIRSE data are shown in Fig. 5 for the homoepitaxial sample. Results from electrical Hall measurements at room temperature are also included in Table I. The free carrier concentration and electron mobility, which is averaged within the monolinic (010) plane, are in very good agreement with the gIRSE best model results. It is noted that the gIRSE analysis provides access to the anisotropy in the mobility parameters. We also note that SIMS results show an [Si] of 2×10^{19} cm^{-3}, which is in agreement with the findings from electrical and optical analyses and suggests a high degree of donor activation. The SIMS results further proved a homogeneous Si distribution within the homoepitaxial layer.

Previous reports of free electron mobility parameters in Si-doped homoepitaxial β-Ga_2O_3 (010) with similar free electron density and grown by MOCVD are also included in Table I.[35,61–63] The results obtained here by the hot-wall MOCVD approach for the electrical mobility parameters compare well with the state-of-the-art values reported previously for similar carrier concentrations.

TABLE I. Room temperature free charge carrier parameters for the homoepitaxial (010) β-Ga_2O_3 layer and β-Ga_2O_3 substrate determined from gIRSE and electrical Hall effect measurements in this work compared with selected data from reports in the literature on Si-doped homoepitaxial (010) β-Ga_2O_3 layers with similar free electron concentrations and grown by MOCVD.

		N cm^{-3}	μ_a $cm^2 V^{-1}s^{-1}$	μ_b $cm^2 V^{-1}s^{-1}$	$\mu_{c^\star}$ $cm^2 V^{-1}s^{-1}$
gIRSE	Epilayer	$(1.4 \pm 0.1) \times 10^{19}$	73 ± 1	42 ± 1	79 ± 1
Electrical Hall	Epilayer	1.9×10^{19}	69[a]	n.a.[b]	69[a]
gIRSE	Substrate	$(2.5 \pm 0.1) \times 10^{17}$	28 ± 1	45 ± 1	36 ± 1
Electrical Hall[c]	Epilayer	1.1×10^{19}	95[a]	n.a.[b]	95[a]
Electrical Hall[d]	Epilayer	2.0×10^{19}	49[a]	n.a.[b]	49[a]
Electrical Hall[e]	Epilayer	1.1×10^{19}	100[a]	n.a.[b]	100[a]
Electrical Hall[f]	Epilayer	1.0×10^{19}	58[a]	n.a.[b]	58[a]

[a]Isotropic average in monoclinic plane.
[b]Out-of-plane mobility parameter not accessible.
[c]Meng *et al.*, Ref. 61.
[d]Bhattacharyya *et al.*, Ref. 35.
[e]Bhattacharyya *et al.*, Ref. 62.
[f]Baldini *et al.*, Ref. 63.

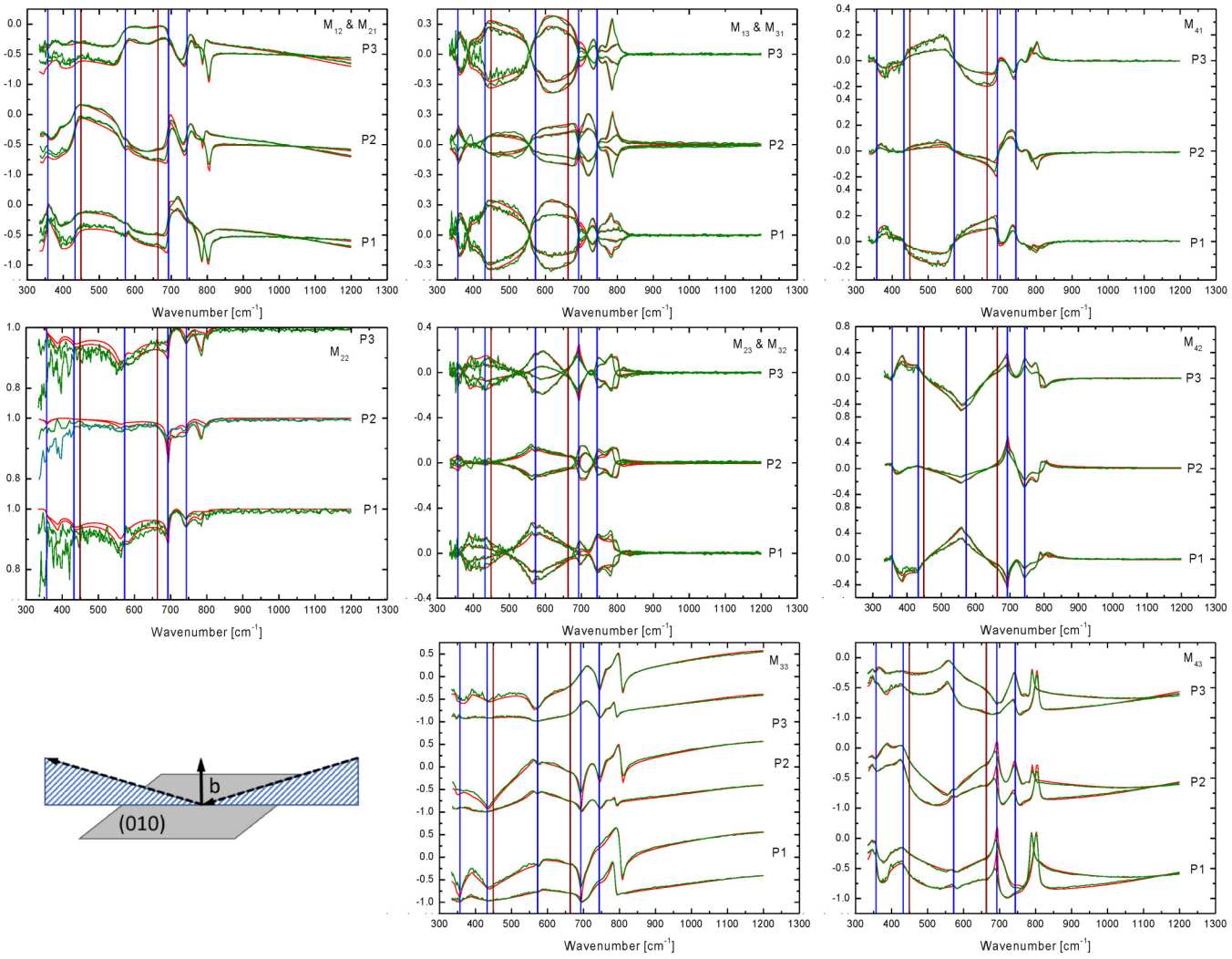

FIG. 5. Experimental (green lines) and best match model calculated (red lines) Mueller matrix data obtained from the β-Ga_2O_3 (010) homoepitaxial layer on (010) substrate sample at three different sample azimuth orientations [P1: ϕ = 16.(1)°, P2: ϕ = -29.(1)°, P3: ϕ = -74.(1)°]. Data were taken at two angles of incidence ($\Phi_a = 50°$, 70°). Mueller matrix data symmetric in their indices are equal and are plotted within the same panels for convenience. Vertical lines indicate wavenumbers of TO phonon modes (solid lines) with B_u symmetry (blue) and A_u symmetry (brown). The last digit which is determined within the 90% confidence interval is indicated with parentheses. All elements M_{ij} are normalized to M_{11}. The remaining Euler angle parameters are set to $\theta = 0°$ and $\psi = 0°$ according to the crystallographic orientation of the (010) surface. The inset depicts schematically the sample surface, the plane of incidence, and the orientation of axis **b**. Euler angles, crystal coordinates, and data analyses procedures are defined and described in Ref. 57.

D. Thermal conductivity

The experimentally determined thermal conductivity values of the representative 540-nm-thick Si-doped β-Ga_2O_3 (010) homoepitaxial layer and the substrate in a temperature range from 80 to 400 K are shown in Fig. 6. Our data for β-Ga_2O_3 (010) substrates are in very good agreement with values measured by time-domain thermoreflectance[64,65] and laser-flash method,[66] as well as with first-principles calculations.[67] The thermal conductivity of the homoepitaxial layer approaches the bulk values at temperatures higher than 200 K. The surprisingly high thermal conductivity obtained for the homoepitaxial layer can be explained by (i) a weak boundary effect as a result of indistinguishable interface between the layer and substrate and (ii) by the low dislocation densities. Similar observation has been reported for homoepitaxially grown GaN layers.[68] At temperatures lower than 150 K, the thermal conductivity of the homoepitaxial layer becomes significantly lower than the bulk values. This result can be explained by the increased contribution of the phonon-impurity scattering rate at low temperature. Note that there are no existing literature data for

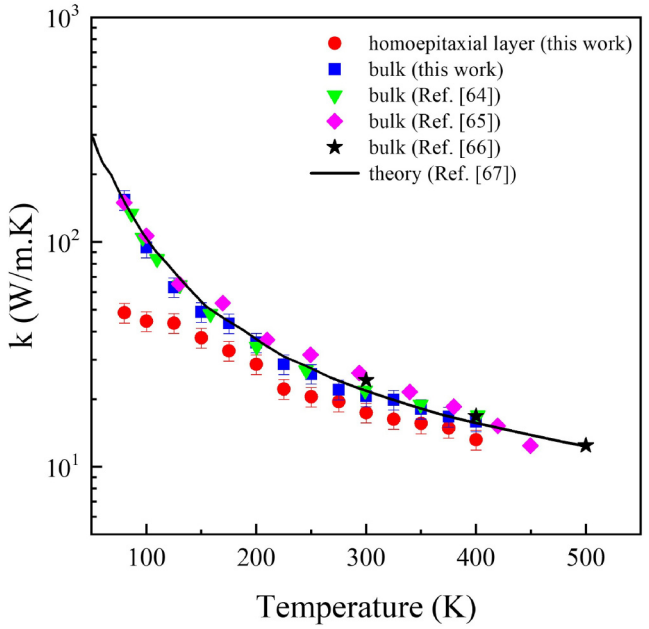

FIG. 6. Thermal conductivity of Si-doped β-Ga_2O_3 (010) homoepitaxial layer and β-Ga_2O_3 (010) substrate. Some of the literature data for thermal conductivity of bulk β-Ga_2O_3 (010) are also plotted. The solid line presents the results from first-principles calculations (Ref. 67).

heteroepitaxial or homoepitaxial β-Ga_2O_3 (010) layers for a direct comparison.

IV. CONCLUSIONS

Growth of high quality β-Ga_2O_3 single-crystalline layers on native β-Ga_2O_3 substrates with (010) surface orientation, based on the hot-wall method, is demonstrated. A very small FWHM of the rocking curve of the (010) peak of 11 arc sec for a 540 nm-thick layer has been achieved, which is even better than that of the Edge defined Film-fed Grown (010) β-Ga_2O_3 substrate (19 arc sec). Furthermore, it is shown that the structural anisotropy is substantially reduced in the layer, hence demonstrating lower structural defect density for epilayers with respect to the bulk substrates. The layer's crystal quality is well correlated with the surface roughness (root mean square roughness value of 0.6 nm over a $5 \times 5\,\mu m^2$ area, which is within the smallest reported in the literature) and a high electron mobility value of 69 $cm^2\ V^{-1}\ s^{-1}$ at a free carrier concentration $n = 1.9 \times 10^{19}\ cm^{-3}$. Furthermore, a new procedure for epi-ready surface preparation of β-Ga_2O_3 (010) substrates by annealing in Ar atmosphere for a very short time interval, instead of typically employed in oxygen, is presented and discussed. Therefore, the hot-wall MOCVD process developed has a large potential for growth of device-relevant β-Ga_2O_3 material.

ACKNOWLEDGMENTS

This work was performed within the framework of the Center for III-Nitride Technology, C3NiT-Janzén, supported by the Swedish Governmental Agency for Innovation Systems (VINNOVA) under the Competence Center Program (Grant No. 2022-03139). We further acknowledge support from the Swedish Research Council under Grant Nos. 2016-00889, 2017-03714, and 2023-04993, the Swedish Foundation for Strategic Research under Grant No. EM16-0024, and the Swedish Government Strategic Research Area in Materials Science on Functional Materials at Linköping University, Faculty Grant SFO Mat LiU (No. 009-00971). M.S. acknowledges support by the National Science Foundation (NSF) under Award No. OIA-2044049, NSF/EPSCoR RII Track-1: Emergent Quantum Materials and Technologies (EQUATE), by Air Force Office of Scientific Research under Award Nos. FA9550-19-S-0003 and FA9550-21-1-0259, by the University of Nebraska Foundation, and by the J. A. Woollam Foundation. V.J. acknowledges the Carl Trygger Foundation (Grant No. 2018-183). We acknowledge Steffen Richter for support with the gIRSE measurements.

AUTHOR DECLARATIONS

Conflict of Interest

The authors have no conflicts to disclose.

Author Contributions

D. Gogova: Conceptualization (equal); Data curation (equal); Formal analysis (equal); Investigation (equal); Methodology (equal); Validation (equal); Writing – original draft (equal); Writing – review & editing (equal). **D. Q. Tran:** Data curation (equal); Formal analysis (equal); Investigation (equal); Software (equal); Validation (equal); Visualization (equal); Writing – original draft (equal); Writing – review & editing (equal). **V. Stanishev:** Data curation (equal); Formal analysis (equal); Investigation (equal); Software (equal). **V. Jokubavicius:** Data curation (equal); **L. Vines:** Data curation (equal); Formal analysis (equal); Writing – review & editing (supporting). **M. Schubert:** Formal analysis (equal); Validation (equal); Visualization (equal); Writing original draft (equal); **R. Yakimova:** Conceptualization (equal); Formal analysis (equal); Writing original draft (supporting); Writing – review & editing (supporting). **P. P. Paskov:** Formal analysis (equal); Supervision (equal); Writing – review & editing (equal). **V. Darakchieva:** Conceptualization (equal); Formal analysis (equal); Funding acquisition (lead); Investigation (equal); Project administration (lead); Resources (lead); Supervision (equal); Writing – original draft (equal); Writing – review & editing (lead).

DATA AVAILABILITY

The data that support the findings of this study are available from the corresponding author upon reasonable request.

REFERENCES

[1]C. G. Grangvist, *Handbook of Inorganic Electrochromic Materials* (Elsevier, Amsterdam, 1995).
[2]E. Fortunato, D. Ginley, H. Hosono, and D. C. Paine, MRS Bull. **32**, 242 (2007).
[3]D. Gogova, A. Iossifova, T. Ivanova, Z. Dimitrova, and K. Gesheva, J. Cryst. Growth **198-199**, 1230 (1999).
[4]M. Fleischer, Meas. Sci. Technol. **19**, 042001 (2008).

[5]A. V. Almaev, E. V. Chernikov, V. V. Novikov, B. O. Kushnarev, N. N. Yakovlev, E. V. Chuprakova, V. L. Oleinik, A. D. Lozinskaya, and D. S. Gogova, J.Vac. Sci. Technol. A **39**, 023405 (2008).
[6]N. Yakovlev *et al.*, IEEE Sens. J. **23**, 1885 (2023).
[7]A. Almaev *et al.*, Chemosensors **11**, 325 (2023).
[8]C. Sturm, J. Furthmüller, F. Bechstedt, R. Schmidt-Grund, and M. Grundmann, APL Mater. **3**, 106106 (2015).
[9]A. Mock, R. Korlacki, C. Briley, V. Darakchieva, B. Monemar, Y. Kumagai, K. Goto, M. Higashiwaki, and M. Schubert, Phys. Rev. B **96**, 245205 (2017).
[10]M. Higashiwaki, AAPPS Bull. **32**, 3 (2022).
[11]X. Ji *et al.*, J. Phys. D: Appl. Phys. **55**, 443002 (2022).
[12]D. Guo, Q. Guo, Z. Chen, Z. Wu, P. Li, and W. Tang, Mater. Today Phys. **11**, 100157 (2019).
[13]Z. Liu and W. Tang, J. Phys. D: Appl. **56**, 093002 (2023).
[14]S. J. Pearton, J. Yang, P. H. Cary, F. Ren, J. Kim, M. J. Tadjer, and M. A. Mastro, Appl. Phys. Rev. **5**, 011301 (2018).
[15]Shivani, D. Kaur, A. Ghosh, and M. Kumar, "A strategic review on gallium oxide based power electronics: Recent progress and future prospects," Mater. Today Commun. **33**, 104244 (2022).
[16]A. Titov, K. Karabeshkin, A. Struchkov, V. Nikolaev, A. Azarov, D. Gogova, and P. Karaseov, Vacuum **200**, 111005 (2022).
[17]A. Nikolskaya *et al.*, J. Vac. Sci. Technol. A **39**, 030802 (2021).
[18]A. Y. Polyakov *et al.*, J. Appl. Phys. **130**, 185701 (2021).
[19]V. P. Chowdam *et al.*, Mater. Today Phys. **35**, 101095 (2023).
[20]H. F. Mohamed, C. Xia, Q. Sai, H. Cui, M. Pan, and H. Qi, J. Semicond. **40**, 011801 (2019).
[21]A. Y. Polyakov, N. B. Smirnov, I. V. Shchemerov, E. B. Yakimov, S. J. Pearton, F. Ren, A. V. Chernykh, D. Gogova, and A. I. Kochkova, ECS J. Solid State Sci. Technol. **8**, Q3019 (2019).
[22]D. Gogova, M. Schmidbauer, and A. Kwasniewski, CrystEngComm **17**, 6744 (2015).
[23]M. J. Tadjer *et al.*, J. Phys. D: Appl. Phys. **54**, 034005 (2021).
[24]D. Gogova, G. Wagner, M. Baldini, M. Schmidbauer, K. Irmscher, R. Schewski, Z. Galazka, M. Albrecht, and R. Fornari, J. Cryst. Growth **401**, 665 (2014).
[25]G. Seryogin, F. Alema, N. Valente, H. Fu, E. Steinbrunner, A. T. Neal, S. Mou, A. Fine, and A. Osinsky, Appl. Phys. Lett. **117**, 262101 (2020).
[26]Z. Feng, A. F. M. Anhar Uddin Bhuiyan, M. R. Karim, and H. Zhao, Appl. Phys. Lett. **114**, 250601 (2019).
[27]D. Gogova *et al.*, AIP Adv. **12**, 055022 (2022).
[28]Z. Li *et al.*, Vacuum **178**, 109440 (2020).
[29]E. Farzana, E. Ahmadi, J. S. Speck, A. R. Arehart, and S. A. Ringel, J. Appl. Phys. **123**, 161410 (2018).
[30]A. Waseem, Z. Ren, H.-C. Huang, K. Nguyen, X. Wu, and X. Li, Phys. Status Solidi A **220**, 2200616 (2023).
[31]A. F. M. A. U. Bhuiyan, Z. Feng, L. Meng, and H. Zhao, J. Appl. Phys. **133**, 211103 (2023).
[32]N. Ma, N. Tanen, A. Verma, Z. Guo, T. Luo, H. G. Xing, and D. Jena, Appl. Phys. Lett. **109**, 212101 (2016).
[33]Z. Zhang, E. Farzana, A. R. Arehart, and S. A. Ringel, Appl. Phys. Lett. **108**, 052105 (2016).
[34]F. Alema, Y. Zhang, A. Mauze, T. Itoh, J. S. Speck, B. Hertog, and A. Osinsky, AIP Adv. **10**, 085002 (2020).
[35]A. Bhattacharyya, P. Ranga, S. Roy, J. Ogle, L. Whittaker-Brooks, and S. Krishnamoorthy, Appl. Phys. Lett. **117**, 142102 (2020).
[36]A. Papamichail *et al.*, J. Appl. Phys. **131**, 185704 (2022).
[37]H. Zhang, J.-T. Chen, A. Papamichail, I. Persson, P. P. Paskov, and V. Darakchieva, J. Cryst. Growth **603**, 127002 (2023).
[38]V. Stanishev, N. Armakavicius, D. Gogova, M. Nawaz, N. Rorsman, P. P. Paskov, and V. Darakchieva, Vacuum **217**, 112481 (2023).
[39]J. T. Chen, I. Persson, D. Nilsson, C. W. Hsu, J. Palisaitis, U. Forsberg, P. O. Persson, and E. Janzén, Appl. Phys. Lett. **106**, 251601 (2015).
[40]P. Gribisch, R. D. Carrascon, V. Darakchieva, and E. Lind, IEEE Trans. Electron Devices **70**, 2408 (2023).
[41]A. Papamichail *et al.*, Appl. Phys. Lett. **122**, 153501 (2023).
[42]D.-Y. Chen, A. R. Persson, V. Darakchieva, P. O. A. Persson, J.-T. Chen, and N. Rorsman, Semicond. Sci. Technol. **38**, 105006 (2023).
[43]Y. S. Touloukian, R. W. Powell, C. Y. Ho, and P. G. Klemens, *Thermophysical Properties of Matters - The TPRC Data Series, Vol. 1 – Thermal Conductivity - Metallic Elements and Alloys* (IFI/Plenum, New York, 1970).
[44]Y. S. Touloukian, R. W. Powell, C. Y. Ho, and P. G. Klemens, *Thermophysical Properties of Matters - The TPRC Data Series, Vol. 4 – Specific Heat - Metallic Elements and Alloys* (IFI/Plenum, New York, 1970).
[45]E. G. King, J. Am. Chem. Soc. **80**, 1799 (1958).
[46]D. Q. Tran, N. Blumenschein, A. Mock, P. Sukkaew, H. Zhang, J. F. Muth, T. Paskova, P. P. Paskov, and V. Darakchieva, Phys. B: Condens. Matter **579**, 411810 (2020).
[47]D. Q. Tran, R. D. Carrascon, M. Iwaya, B. Monemar, V. Darakchieva, and P. P. Paskov, Phys. Rev. Mater. **6**, 104602 (2022).
[48]D. Gogova, V. S. Olsen, C. Bazioti, I.-H. Lee, O. Prytz, L. Vines, and A. Y. Kuznetsov, CrystEngComm **22**, 6268 (2020).
[49]D. Gogova, H. Larsson, R. Yakimova, Z. Zolnai, I. Ivanov, and B. Monemar, Phys. Status Solidi A **200**, 13 (2003).
[50]A. Okada, M. Nakatani, L. Chen, R. A. Ferreyra, and K. Kadono, Appl. Surf. Sci. **574**, 151651 (2022).
[51]S. Ohira, N. Arai, T. Oshima, and S. Fujita, Appl. Surf. Sci. **254**, 7838 (2008).
[52]V. Stanishev, N. Armakavicius, C. Bouhafs, C. Coletti, P. Kühne, I. G. Ivanov, A. A. Zakharov, R. Yakimova, and V. Darakchieva, Appl. Sci. **11**, 1891 (2021).
[53]V. Darakchieva *et al.*, J. Appl. Phys. **108**, 073529 (2010).
[54]X. Ma, R. Xu, J. Xu, L. Ying, Y. Mei, H. Long, and B. Zhang, J. Appl. Crystallogr. **54**, 1153 (2021).
[55]A. Kuramata, K. Koshi, S. Watanabe, and Y. Yamaoka, "Floating zone method, edge-defined film-fed growth method, and wafer manufacturing," in *Gallium Oxide: Crystal Growth, Materials Properties, and Devices*, edited by M. Higashiwaki and S. Fujita (Springer Nature Switzerland AG, Springer Cham, 2020).
[56]K. Hanada, T. Moribayashi, K. Koshi, K. Sasaki, A. Kuramata, O. Ueda, and M. Kasu, Jpn. J. Appl. Phys. **55**, 1202BG (2016).
[57]M. Schubert *et al.*, Phys. Rev. B **93**, 125209 (2016).
[58]M. Schubert, Phys. Rev. Lett. **117**, 215502 (2016).
[59]S. Knight, A. Mock, R. Korlacki, V. Darakchieva, B. Monemar, Y. Kumagai, K. Goto, M. Higashiwaki, and M. Schubert, Appl. Phys. Lett. **112**, 012103 (2018).
[60]M. Schubert *et al.*, Appl. Phys. Lett. **114**, 102102 (2019).
[61]L. Meng, Z. Feng, A. F. M. A. U. Bhuiyan, and H. Zhao, Cryst. Growth Des. **22**, 3896 (2022).
[62]A. Bhattacharyya, C. Peterson, T. Itoh, S. Roy, J. Cooke, S. Rebollo, P. Ranga, B. Sensale-Rodriguez, and S. Krishnamoorthy, APL Mater. **11**, 021110 (2023).
[63]M. Baldini, M. Albrecht, A. Fiedler, K. Irmscher, R. Schewski, and G. Wagner, ECS J. Solid State Sci. Technol. **6**, Q3040 (2016).
[64]P. Jiang, X. Qian, X. Li, and R. Yang, Appl. Phys. Lett. **113**, 232105 (2018).
[65]Z. Cheng, N. Tanen, C. Chang, J. Shi, J. McCandless, D. Muller, D. Jena, H. G. Xing, and S. Graham, Appl. Phys. Lett. **115**, 092105 (2019).
[66]D. Klimm, B. Amgalan, S. Ganschow, A. Kwasniewski, Z. Galazka, and M. Bickermann, Cryst. Res. Technol. **58**, 2200204 (2023).
[67]M. D. Santia, N. Tandon, and J. D. Albrecht, Appl. Phys. Lett. **107**, 041907 (2015).
[68]Y. R. Koh *et al.*, Phys. Rev. Mater. **5**, 104604 (2021).